International Journal of *Geo-Information*

MDPI

Article

Spatiotemporal Relationship Between Land Subsidence and Ecological Environmental Quality in Shenfu Mining Area, Loess Plateau, China

Shuaizhi Kang [1], Xia Jia [2], Yonghua Zhao [1,*], Yong Ao [1] and Chaoqun Ma [1]

[1] School of Land Engineering, Key Laboratory of Degraded and Unused Land Consolidation Engineering of the Ministry of Natural Resources, Shaanxi Key Laboratory of Land Consolidation, Shaanxi Provincial Land Consolidation Engineering Technology Research Center, Chang'an University, Xi'an 710054, China; 2020035002@chd.edu.cn (S.K.); aoyong@chd.edu.cn (Y.A.); chaoqunm@chd.edu.cn (C.M.)

[2] School of Water and Environment, Chang'an University, Xi'an 710054, China; jiaxia@chd.edu.cn

* Correspondence: yonghuaz@chd.edu.cn

Abstract: The exploitation of coal resources has caused problems such as ground deformation, affecting the ecological environment. Spatiotemporal varying characteristics between land subsidence and ecological environmental quality (EEQ) are an important research hotspot. Using the SBAS-InSAR method, 64 Sentinel-1 images were utilized to monitor land subsidence in the Shenfu mining area, one of China's largest coal source regions. And the remote sensing ecological index (RSEI) was used to monitor and evaluate EEQ of the Shenfu mining area. Global and local spatial autocorrelation methods were used to assess the spatial aggregation degree and change patterns over time. Spatial Econometric Models were employed to explore the impacts of land subsidence on EEQ. The results showed the following: (1) The average RSEI values in the Shenfu mining area were 0.531, 0.488, and 0.523 in 2016, 2018, and 2020, respectively; there was a slight downward trend in EEQ. The permanent scatter (PS) point deformation rate ranged from −353.40 mm/year to +246.24 mm/year, with average deformation rates of 0.1642, 0.2181, and 0.2490 mm/year, respectively. (2) There was a significant correlation and spatial agglomeration effect between land surface subsidence and EEQ. Low–high, high–low, and low–low clusters were the main types of relationships, indicating that land subsidence primarily has a negative spatial impact on the ecological environment. (3) The relationship between land subsidence and EEQ varied spatially in the Shenfu mining area at 500 × 500 grid units. This research can provide scientific guidance for disaster prevention and sustainable development in mining areas by considering long-term differences in ecological environmental quality and its correlation with land subsidence.

Keywords: land subsidence; ecological environmental quality; SBAS-InSAR; Shenfu mining area

check for updates

Citation: Kang, S.; Jia, X.; Zhao, Y.; Ao, Y.; Ma, C. Spatiotemporal Relationship Between Land Subsidence and Ecological Environmental Quality in Shenfu Mining Area, Loess Plateau, China. *ISPRS Int. J. Geo-Inf.* **2024**, *13*, 390. https://doi.org/10.3390/ijgi13110390

Academic Editors: Wolfgang Kainz, Dimitrios D. Alexakis and Adrianos Retalis

Received: 29 June 2024
Revised: 8 October 2024
Accepted: 28 October 2024
Published: 31 October 2024

1. Introduction

In the past, coal was a key factor in the national development and growth of the energy structure of different countries [1,2]. Coal has also made an important contribution to economic and social advances worldwide [3,4]. Most mining-related geologic hazards were directly caused by mining activities, such as landslides, infrastructure damage, land subsidence, etc., ultimately posing a catastrophic risk to society and the economy [5,6]. Coal mining activities caused significant damage and land subsidence was one of the most alarming disasters [7,8], seriously harming the fragile ecology and environment of the mining area [9]. Thus, the identification of their relationship and spatiotemporal change characteristics was an essential issue for regional planning and management [10–12].

Various methods were applied to monitor land subsidence [13–16]. The InSAR method was cost-effective and efficient, and excellently applied in previous research [17–19], providing an all-day, all-weather surveying option for large-scale regions. Time series analysis of InSAR data was an important tool for monitoring and measuring earth surface displacement [20]. Recent research has shown that land subsidence can be detected with SAR remote sensing data using various InSAR methods. D-InSAR, PS-InSAR, and SBAS-InSAR were compared for monitoring mining region subsidence, with SBAS-InSAR showing the best performance [21]. In addition, SBAS-InSAR was widely used to monitor and analyze the spatial and temporal evolution of land subsidence in previous research [22]. Therefore, the SBAS-InSAR method was chosen for this study as an effective tool to analyze the spatiotemporal patterns of land subsidence. Remote sensing data have been increasingly used due to their rapid, objective, and large-scale real-time monitoring capabilities for observing the ecological environment. The remote sensing ecological index (RSEI) can be calculated using remote sensing data and consists of four key indicators representing how humans intuitively perceive ecological conditions: greenness, humidity, heat, and dryness [23]. The RSEI was widely used in past studies in areas with diverse ecological conditions, such as urban [24], mountainous [25], basin [26], and mining areas [27]. Some studies focused on EEQ evaluation and land subsidence in mining areas [27–29]. EEQ within a unit was influenced not only by the ecosystem health level of the unit itself but also by the ecosystem health levels of adjacent or distant units, and other factors [30]. However, it was crucial to combine different data and methods to analyze land deformation and EEQ. Spatial regression methods were effective for exploring the spatial and temporal variations in the complex relationships between multiple variables such as habitat quality, landscape ecology, and land use [30–35].

The Shenfu mining area with abundant coal reserves was a very important coal source in the Loess plateau, China, and has developed rapidly in recent years. The annual extraction of coal mines resulted in significant impacts on the land environment [36]. Meanwhile, increasing populations and development activities continuously put more pressure on the local land ecosystem. Given the lack of current research, we focused on the Shenfu mining area, which faces ecological security risks, as the sample area for our study. This study aimed to address the following scientific questions: (1) Was land subsidence widely distributed in the Shenfu mining area? (2) What were the spatial characteristics of land subsidence in the Shenfu mining area? (3) Was there spatial correlation between land subsidence and EEQ? These results can improve the understanding of ground deformation caused by mining activities, which is helpful in guiding disaster prevention, mitigation, and the management and development of coal mining areas.

2. Materials and Methods

2.1. Study Area

The Shenfu mining area (109°37′30″~110°49′30″ E, 38°32′00″~39°28′00″ N) is located in the northern Shaanxi Province, a hilly area of the Loess plateau, which is a typical transitional area with a temperate semiarid continental monsoon climate close to the Mu Us Desert (Figure 1), including Shenmu County and Fugu County. The land area measures about 10,864 km^2, with elevations in the range of 718–1437 m and slopes in the range of 0–47.67°. The annual average temperature is 8.4 °C. The average annual precipitation of the recent year was 410.3 mm, with the majority falling in the summer and autumn.

The mineral resources in the study area were mainly coal mines, including one of the largest coal fields in China. The local area is rich in mineral resources, of which coal reserves were the most abundant and the coal quality was excellent with shallow burials and easy to mine. According to the work report of the local energy bureau in 2020, the coal production of Shenmu County and Fugu County was 1.24×10^8 t/a and 0.9×10^8 t/a of the total design capacity, respectively, and the combined coal production accounted for about 13% of the national coal production in that year, which was a typical high-intensity coal mining area. Historically, mining activities were an important source of energy and industrial consumption in the local region. Additionally, the characteristics of the LP's soil lead to frequent geological disasters, posing potential risks to human settlements in the study area.

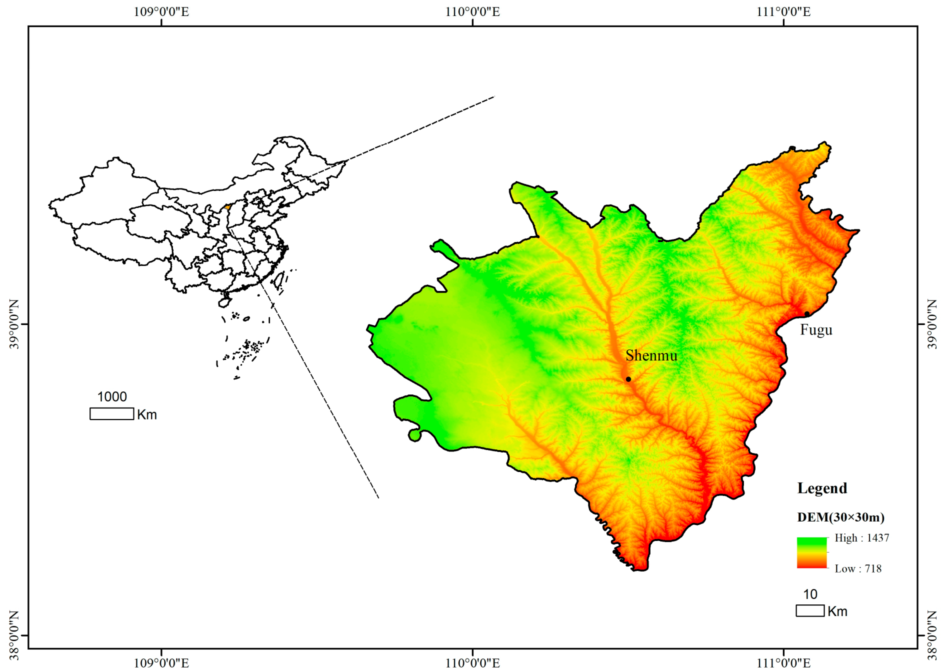

Figure 1. Location and DEM of the study area.

2.2. Data Collection and Preprocessing

Landsat 8 satellite remote sensing data with a 30 m spatial resolution were obtained from the Tier 1 dataset on GEE (https://earthengine.google.com/), meeting both geometric and radiometric quality standards. We used data from 1 June to 31 September with cloud cover lower than 20%. In total, 64 scenes ascending Sentinel-1 satellite single look complex (SLC) data with the Interferometric Wide swath (IW) model and the precise orbit determination (POD) data from 2018 to 2020 were acquired freely from the European Space Agency (ESA) Copernicus Open Access Hub website (https://scihub.copernicus.eu). Shuttle Radar Topographic Mission (SRTM) DEM data with the same spatial resolution as Landsat 8 data were acquired from the CGIAR-CSI SRTM (http://srtm.csi.cgiar.org/). All the data used and the sources are shown in Table 1. The framework of this study is as follows (Figure 2).

Table 1. Datasets used in this study.

Data	Resolution	Date	Source
Sentinel-1	2.3 m, azimuth 14 m	2016–2020	https://scihub.copernicus.eu/
DEM	30 m	2000	http://srtm.csi.cgiar.org
Landsat-8	30 m	2016–2020	https://earthengine.google.com/

2.3. Methodology

2.3.1. SBAS-InSAR

Multitemporal SAR data were implemented using the Small Baseline Subset (SBAS) InSAR approach [37] with ENVI5.3 within SARScape module version 5.2.1. The SBAS-InSAR method improved the monitoring accuracy [38,39]. First, based on baseline threshold values, an appropriate combination of differential interferograms was produced by SAR data pairs. Then, the deformation data of every single differential interferogram was estimated and regarded as the observed values. Ultimately, all deformation information with time series was retrieved based on the observed values obtained in the previous process [40]. The principle can be demonstrated by the following equations:

$$\frac{N+1}{2} \leq M \leq N\left(\frac{N+1}{2}\right) \tag{1}$$

$$\begin{aligned} \phi_j(x,r) &= \phi(t_B,x,r) - \phi(t_A,x,r) \\ &\approx \Delta\phi_{\text{disp}} + \Delta\phi_{\text{topo}} + \Delta\phi_{\text{orb}} + \Delta\phi_{\text{atm}} + \Delta\phi_{\text{noise}} \end{aligned} \tag{2}$$

$$A\phi = \delta\phi \tag{3}$$

$$v = [v_1, v_2, \cdots v_N]^T = \left[\frac{\phi_1}{t_1 - t_0}, \frac{\phi_2 - \phi_1}{t_2 - t_1}, \cdots, \frac{\phi_N - \phi_{N-1}}{t_N - t_{N-1}}\right]^T \tag{4}$$

where M is the number of differential interferometric pairs; N + 1 is the number of original SAR images. Equation (2) represents the unwrapping phase of a high-coherence point (x, y) of the i-th unwrapping interferogram (corresponding to two moments t_1 and t_2). A refers to a coefficient matrix of $M \times N$. v is the mean phase velocity.

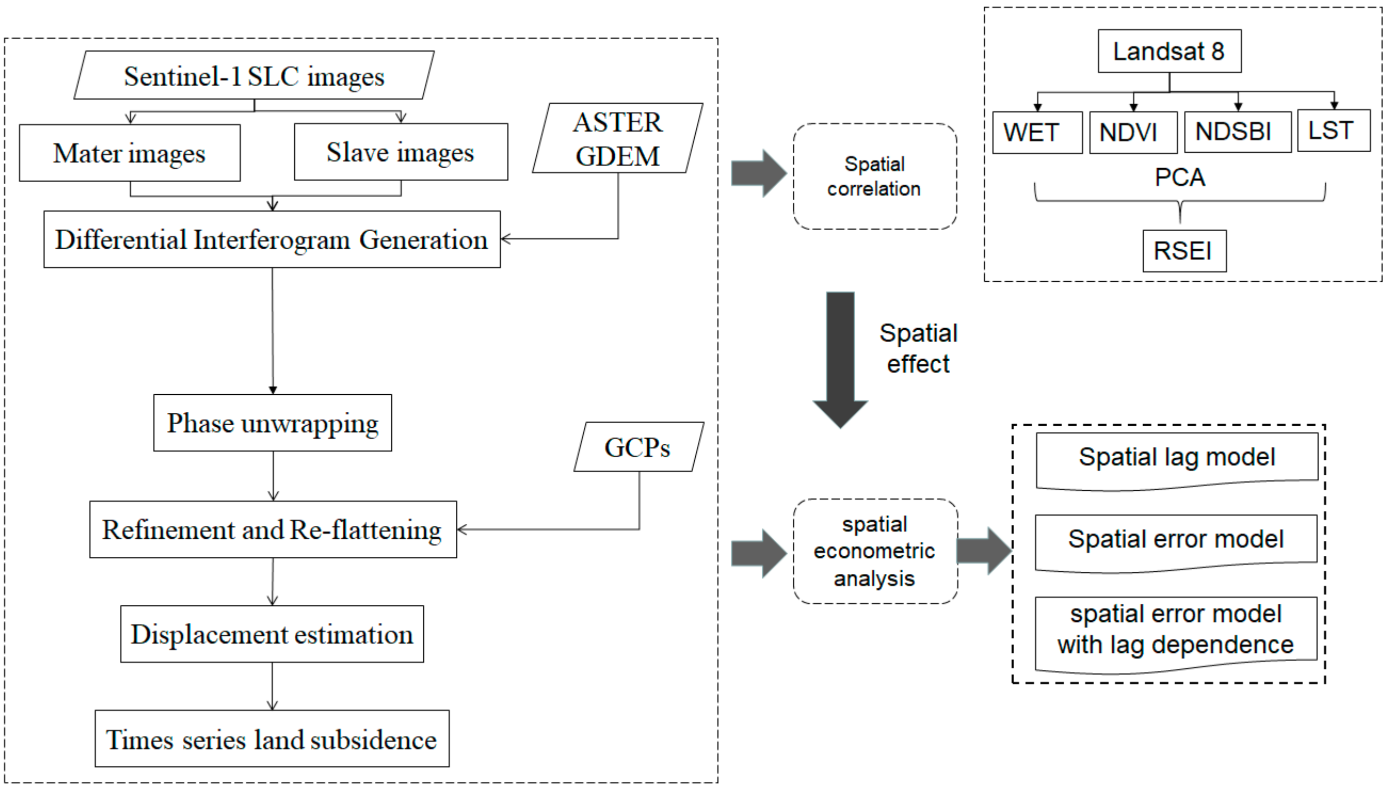

Figure 2. The framework of this study.

After the mosaic and clip process, the SAR data were imported into the connection graph module. The 45% maximum spatial baseline and 365-day maximum temporal baseline were constrained to generate connection diagrams. The Goldstein filtering method was used to remove speckle noise from the images. The all spatial–temporal baseline connectivity maps are shown in Figure 3. The minimum cost flow was adopted in phase unwrapping by the unwrapping coherence threshold of 0.35. Then, 40 ground control points (GCPs) were established to revise the interferometric phase and unwrapped phase. The logical selection was as follows: (1) the location had a high coherence value and good phase unwrapping, (2) the value of deformation was close to zero; (3) GCP 20 was selected ultimately. After two steps of inversion, the result was geocoded. Finally, the deformation rate was mapped over the study area from PS points by kriging interpolation.

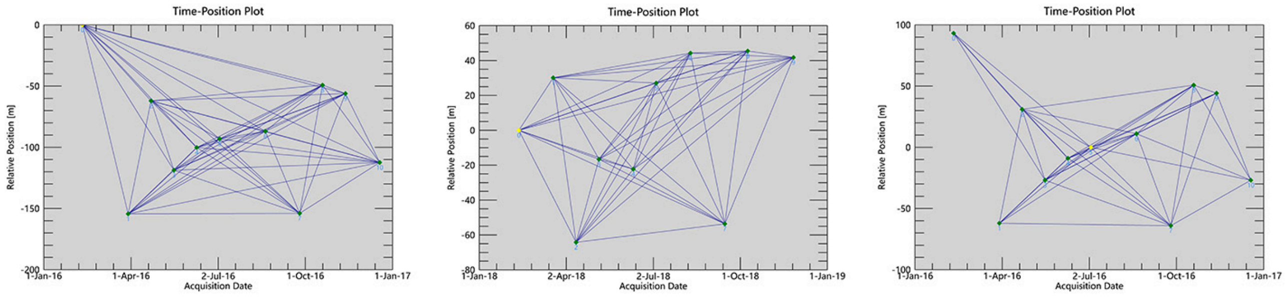

(a) 2016 (b) 2018 (c) 2020

Figure 3. The spatiotemporal baselines (**a**) 2016; (**b**) 2018; (**c**) 2020.

2.3.2. Calculation of the RSEI

Based on the RSEI [41], the normalized difference vegetation index (NDVI) was selected to indicate that the greenness index reflects vegetation growth and its distribution density in the region [42]. The normalized difference soil index (NDSBI) was obtained by means of the index-based built-up index (IBI) and soil index (SI), which reflected the spectral response of land desertification and urbanization [43]. Land surface temperature (LST) was obtained by a single-window algorithm, which reflected the heat indicator [44]. The WET was calculated by the tasselled cap transformation (TCT), which reflected land degradation by the soil water content [45]. All indexes were computed on the Google Earth Engine platform.

$$\mathrm{NDVI} = (\rho_{\mathrm{NIR}} - \rho_{\mathrm{Red}})/(\rho_{\mathrm{NIR}} + \rho_{\mathrm{Red}}) \tag{5}$$

$$\begin{aligned}\mathrm{Wet}_{\mathrm{OLI}} = 0.1511\rho_{\mathrm{blue}} + 0.1973\rho_{\mathrm{green}} + 0.3283\rho_{\mathrm{red}} + 0.3407\rho_{\mathrm{NIR}} \\ -0.7117\rho_{\mathrm{SWIR}_1} - 0.4559\rho_{\mathrm{SWIR}_2}\end{aligned} \tag{6}$$

$$\mathrm{LST} = \mathrm{T}/(1 + (\lambda\mathrm{T}/\rho)\ln\varepsilon) - 273.13 \tag{7}$$

$$\begin{aligned}\mathrm{SI} = \frac{1}{2}\Bigg(&\frac{\rho\_\mathrm{Swir1} + \rho\_\mathrm{Red} - \rho\_\mathrm{Blue} + \rho\_\mathrm{Nir}}{\rho_{\mathrm{Swir1}} + \rho_{\mathrm{Red}} + \rho_{\mathrm{Blue}} + \rho_{\mathrm{Nir}}} \\ &+ \frac{\frac{2\rho_{\mathrm{Swir1}}}{\rho_{\mathrm{Swir1}} + \rho_{\mathrm{Nir}}} - \frac{\rho_{\mathrm{Nir}}}{\rho_{\mathrm{Nir}} + \rho_{\mathrm{Red}}} + \frac{\rho_{\mathrm{Green}}}{\rho_{\mathrm{Green}} + \rho_{\mathrm{Swir1}}}}{\frac{2\rho_{\mathrm{Swir1}}}{\rho_{\mathrm{Swir1}} + \rho_{\mathrm{Nir}}} + \frac{\rho_{\mathrm{Nir}}}{\rho_{\mathrm{Nir}} + \rho_{\mathrm{Red}}} + \frac{\rho_{\mathrm{Green}}}{\rho_{\mathrm{Green}} + \rho_{\mathrm{Swir1}}}}\Bigg)\end{aligned} \tag{8}$$

$$RSEI_0 = 1 - \{PC_1[f\ (Wet,\ NDVI,\ NDSI,\ LST)]\}, \tag{9}$$

$$NI_i = \frac{I_i - I_{min}}{I_{max} - I_{min}} \tag{10}$$

$$\mathrm{RSEI} = \frac{RSEI_0 - RSEI_{min}}{RSEI_{max} - RSEI_{min}} \tag{11}$$

where ρ is the surface reflectance bands; blue, green, red, Nir, Smir_1 and Smir_2 are the Landsat bands at red, blue and green, near-infrared, shortwave infrared 1 and 2, respectively; PC_1 is the first principal component using principal component analysis (PCA); NI_{i} is the standardized value of each index; and RSEI means the $RSEI_0$ that was normalized.

2.3.3. Spatial Correlation Analysis

Spatial autocorrelation was regarded as the coincidence of value similarity with location similarity and utilized to explore patterns of spatial association [46]. A higher positive Moran's I indicates clustering of similar values in neighboring positions, while a lower negative Moran's I suggests an interspersion of higher and lower values; when Moran's I approaches zero, it signifies no spatial clustering, indicating random data distribution, with the significance of the global Moran's I index assessed using the Z-score and *p*-value [47].

The equations for the global Moran's I index area are as follows:

$$\mathrm{y} = \beta_0 + \sum\nolimits_{i=1}^{k} \beta_i x_i + \varepsilon, \tag{12}$$

Local Moran's I is expressed as follows:

$$I_i = \frac{y_i - \overline{y}}{\frac{1}{n}\sum(y_j - \overline{y})^2}\sum_{j\neq i}^{n} w_{ij}(y_j - \overline{y}), \tag{13}$$

where I_i is Moran's I coefficient, n is the whole number of all areas in the study area; w_{ij} indicates the spatial weight, which is represented based on a distance weighting between Z_i and Z_j [48].

The LISA coefficient was utilized to assess the spatial clustering in the land deformation of the study area. Similar to the global Moran's I index, Anselin Local Moran's I statistic ranges from −1 to 1, with the Z-score and p-value used to test its statistical significance, and the results are presented as spatial clusters (high–high and low–low clusters) and spatial outliers (high–low and low–high outliers) in specific locations [49,50].

2.3.4. Spatial Regression Analysis

Spatial econometric models were utilized to solve the complex spatial interaction and spatial dependence between EEQ and land subsidence [51–53]. First, the ordinary least square method was used to detect the relationship between EEQ and land subsidence as a whole, without considering the spatial impact of adjacent areas. Then, a spatial constant coefficient regression model for cross-sectional data was used to explore the spatial relationship between the value of EEQ and land subsidence [54–56]

Ordinary least squares (OSL) is expressed as follows:

$$\mathrm{y} = \beta_0 + \sum_{i=1}^{k} \beta_i x_i + \varepsilon, \tag{14}$$

where x_i and y are the independent variables and β_0 and β_i are the intercept and coefficient, respectively. k represents the number of independent variables; ε is the error term.

The SLM is expressed as follows:

$$y_{it} = \delta\sum_{j=1}^{n} w_{ij}y_{jt} + \beta x_{it} + \mu_i + \lambda_t + \varepsilon_{it}, \varepsilon_{it} \sim i.i.d(0, \delta^2), \tag{15}$$

where i is the cross-section dimension, i = 1, 2, 3. . . n; T means the time dimension, t = 1, 2, 3. . . T; δ represents the coefficient of spatial autoregressive; y_{it} represents the observed value of the explained variable at period T of the i-th section unit; x_{it} is a K-dimensional row vector representing the observed values of k explanatory variables at period t of the i section element; and β is a k-dimensional column vector representing the coefficients of the corresponding explanatory variables. M_i represents the spatial fixation effect, which controls all spatially fixed and time-invariant variables. λ_t represents the time-fixed effect, which controls all variables that are time-fixed and spatially invariant. w_{ij} represents an element of the spatial weight matrix w.

Spatial error model (SEM) is expressed as follows:

$$y_{it} = \beta x_{it} + \mu_i + \lambda_t + \varphi_{it}, \varphi_{it} = \rho\sum_{j=1}^{n} w_{ij}\varphi_{it} + \varepsilon_{it}, [\varepsilon_{it} \sim i.i.d(0, \delta^2)] \tag{16}$$

where φ_{it} is the spatial autocorrelation error term; ρ is the spatial autocorrelation coefficient of the error term.

3. Results

3.1. Spatiotemporal and Change Trends of Land Subsidence and RSEI

Spatial distribution maps of land subsidence, reclassified through multi-temporal analysis of ascending datasets from 2016, 2018, and 2020, are shown in Figure 4. The total number of generated permanent scatter (PS) points was 692,094 in 2016, 595,853 in 2018, and 571,111 in 2020. All PS points were calculated by the kriging interpolation method. During these three periods, the deformation rate ranged from −161.7 to 131.2 mm/year (mm/yr). The annual average deformation rates were 0.1642, 0.2181, and 0.2490 mm/yr in

2016, 2018, and 2020, respectively. The primary land subsidence districts were located in mining areas and built-up regions, mainly along the edges of factories and urban land. The dominant level of slight subsidence points (0–2.5 mm/yr) accounted for 25% or more. The next most distributed deformation points were the extreme level (greater than 10 mm/yr) and minor level (2.5–5 mm/yr), accounting for 23% and 22%, respectively. Moderate deformation points (5–7.5 mm/yr) accounted for 16%, while intense deformation points (7.5–10 mm/yr) had a low distribution, covering 11% of the total area.

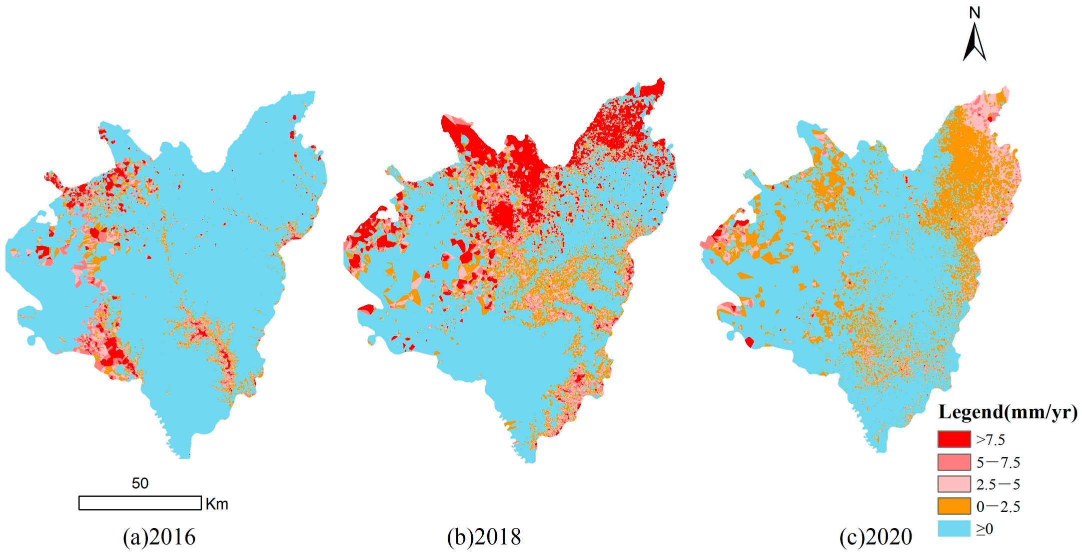

Figure 4. Spatial distribution characteristics of land subsidence (2016–2020) in Shenfu mining area.

The average RSEI values were approximately 0.531, 0.488, and 0.523 in 2016, 2018, and 2020, respectively. This finding indicated that the EEQ of the Shenfu mining area improved significantly over the past five years. The spatial distribution of the reclassified five-degree RSEI and its change from 2016 to 2020 are shown in Figure 5. In terms of spatial distribution characteristics, significant spatial heterogeneity was found in the EEQ of the Shenfu mining area. Specifically, the value of RSEI in a large number of areas was mostly below 0.6, especially the RSEI around the mining industrial area, which was significantly below 0.4. The RSEI in the surrounding mountainous areas was mostly above 0.6. These indicated that human activities, industrial development, urban expansion and EEQ were closely related.

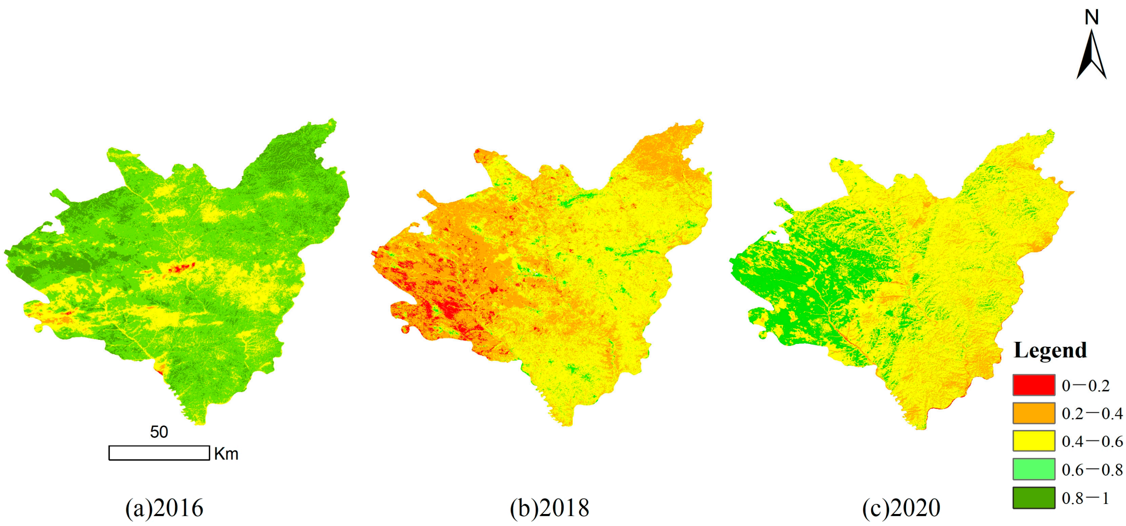

Figure 5. Spatial distribution of RSEI (2016–2020) in Shenfu mining area.

3.2. Spatial Autocorrelation of Land Subsidence and RSEI

A total of 42,578 grid units were created for analysis in the study area, with a distance of 500 km^2. The global Moran's I of land subsidence was 0.759, 0.772, and 0.730 in 2016, 2018, and 2020, respectively (Figure 6). After 999 randomizations, all results passed the significance test ($Z > 1.96$, $p < 0.05$). All had positive spatial correlation. For significance statistical tests for the three periods, global Moran's I all passed at the 99% confidence level across Z scores and p values; there was a significantly global spatial autocorrelation of land subsidence. The global Moran's I index of EEQ was 0.856, 0.679, and 0.493 in 2016, 2018, and 2020, respectively (Figure 7). It showed that there were positive spatial correlations in land subsidence in 2016, 2018, and 2020. In addition, the spatial distribution of land subsidence was more concentrated in the western region in 2018. All data were spatially analyzed by zonal statistics at the same scale of 500 × 500 km. The decrease in the Moreland index of land subsidence and EEQ indicates a reduction in the spatial concentration of land subsidence and EEQ from 2018 to 2020.

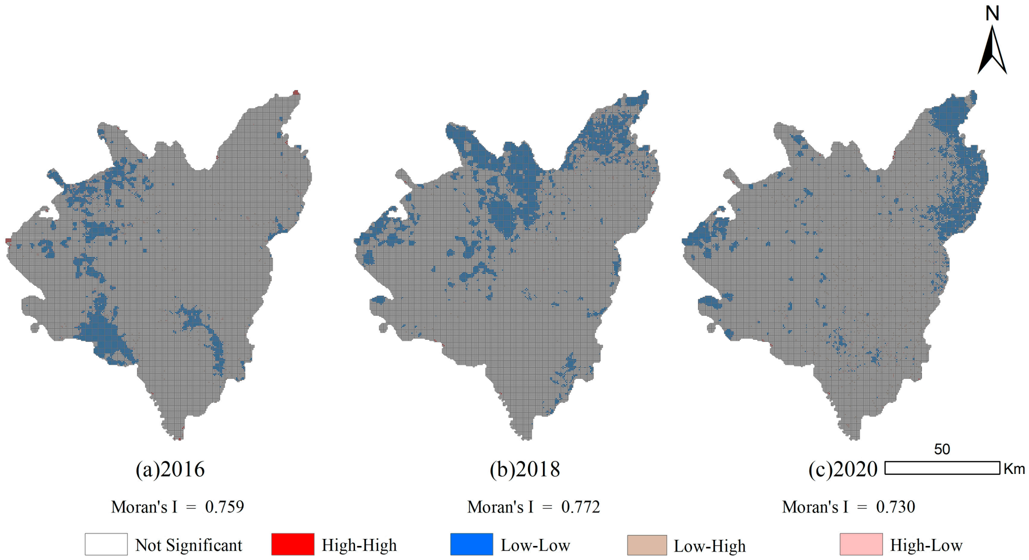

Figure 6. Local indicator of spatial autocorrelation for land subsidence (2016–2020) in Shenfu mining area.

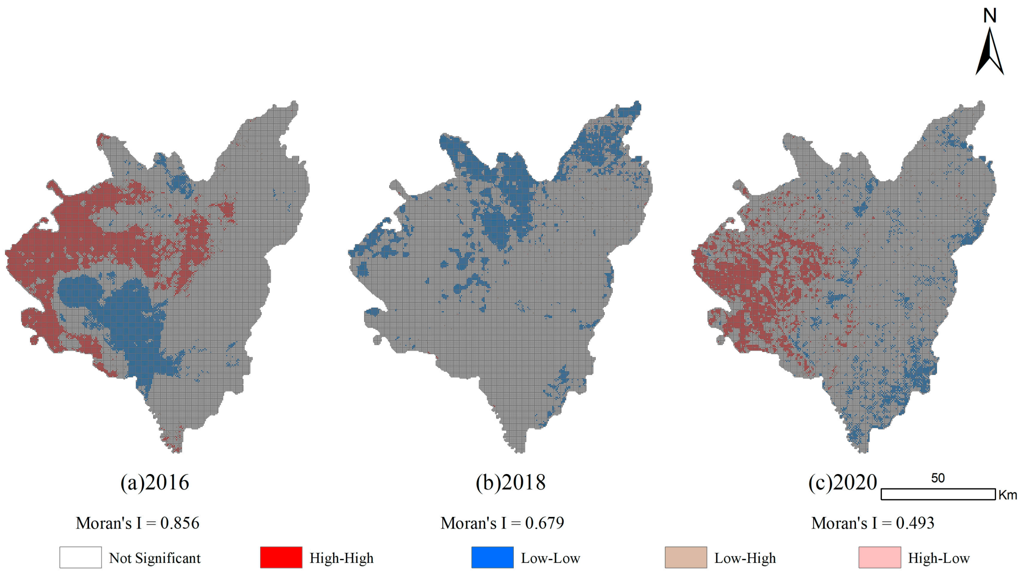

Figure 7. Local indicator of spatial autocorrelation for EEQ (2016–2020) in Shenfu mining area.

3.3. Spatial Associations Between Land Subsidence and EEQ

The spatial associations showed three distinct patterns of spatial heterogeneity in the relationships between land subsidence and EEQ (Figure 8). All global Moran's I indices of spatial associations were −0.100, −0.137, and −0.052, respectively. The results of global bivariate spatial autocorrelation showed that all Moran's I indices were less than 0 and significant at the 0.001 level, which strongly proved that the increase in land subsidence in the Shenfu mining area led to the deterioration of EEQ. During the study period, there was a significant negative spatial correlation between land subsidence and EEQ, indicating that land subsidence influenced the deterioration of EEQ.

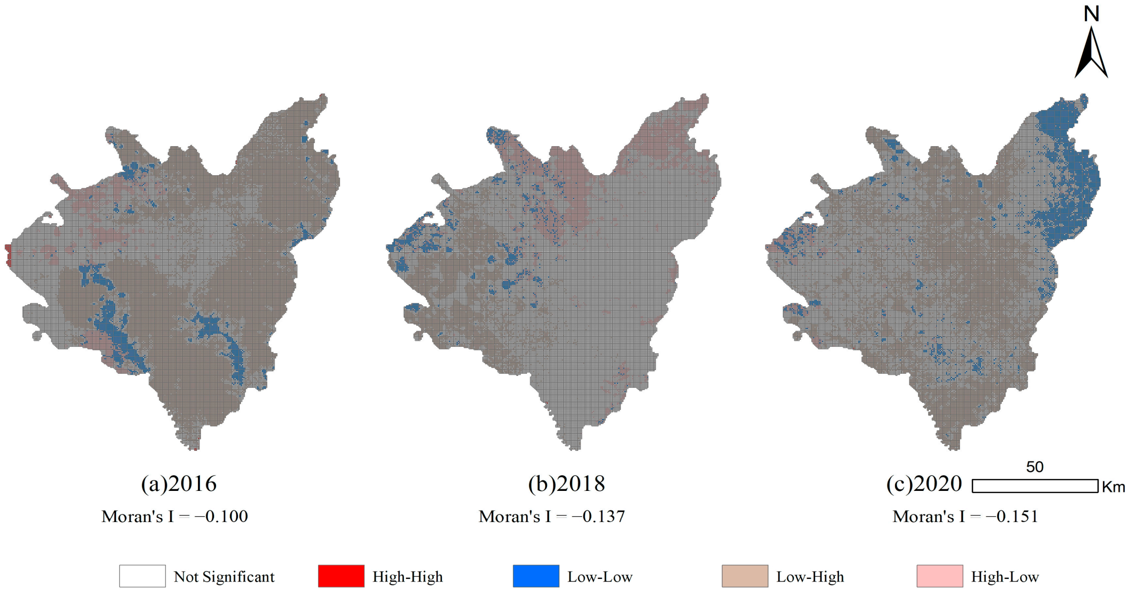

Figure 8. Bivariate local indicators of spatial associations between land subsidence and EEQ (2016–2020) in Shenfu mining area.

According to the bivariate spatial autocorrelation test, there was a significant spatial dependence effect between EEQ and land subsidence, as well as a significant negative externality during the study period. Based on local bivariate spatial autocorrelation analysis, LH type (low ground subsidence rate and high RSEI), HL type (high ground subsidence rate and low RSEI) and LL type (low ground subsidence rate and low RSEI) were the main relationship types between land subsidence and EEQ. This was basically due to the rapid expansion of construction land with the development of the mining industry, which caused a strong disturbance to EEQ. Specifically, the LH type was mostly located in coal mining areas, mainly due to land subsidence caused by coal mining activities in this part of the region. At the same time, from human green mine construction to the restoration of the ecological environment, EEQ was improved. The HL type was located in the developed areas of the chemical industry in Southwest China, mainly because of the flat terrain and high level of economic development in this part of the region. Human activities had a drastic impact on the ecosystem, resulting in the degradation of ecosystem service function and low RSEI value. The LL type was distributed sporadically in urban areas, groundwater exploitation and urban construction caused land subsidence, and the RSEI value was low. There was almost no HH type in the study area, mainly because land subsidence did affect the local EEQ.

3.4. Impact of Land Subsidence on EEQ

Following the bivariate global spatial autocorrelation analysis between EEQ and deformation rates, it was clear that there was a significant spatial dependence between land subsidence and EEQ. Therefore, spatial econometric models were used to estimate and verify the relationship between them. A series of regression models were used to study the impact of land subsidence on the EEQ in order to further investigate the relationship between the EEQ and land subsidence.

SEM, SLM and SEMLD spatial regression models were compared (Table 2). First, OLS analysis was performed without considering spatial interaction. The results of the OLS regression analysis showed that there was a significant spatial dependence between the change in EEQ and the change in land subsidence, implying that the OLS regression model results did not fully or scientifically explain the relationship. By comparing the Log Likehood (LogL), Akaike info criterion (AIC) and Schwarz criterion (SC) values of the three models, the LogL value of the SEMLD model was larger (Table 3), while the AIC and SC values were smaller (Table 4), indicating that SEMLD had strong explanatory power. The spatial regression results showed that the spatial regression model significantly improved the expositive capacity of the model, so the spatial regression model was used in this study.

Table 2. Regression results of ordinary least squares (OLS).

Variables	2016	2018	2020
EEQ	−0.123072	−0.277877	−0.0697017
Constant	0.893254	0.828326	0.776183
Moran's I (error)	0.7553	0.7618	0.7276
Lagrange Multiplier (lag)	47,906.5551	48,941.7824	44,492.2989
Robust LM (lag)	63.8730	292.6878	88.2116
Lagrange Multiplier (error)	47,856.4524	48,680.0793	44,404.2520
Robust LM (error)	13.7703	30.9848	0.1647
Lagrange Multiplier (SARMA)	47,920.3254	48,972.7672	44,492.4636
Log Likelihood	11,119.9	7690.48	20,864.4
Akaike info criterion	−22,235.8	−15,385	−41,724.7
Schwarz criterion	−22,218.5	−15,402.3	−41,707.4
R-squared	0.009878	0.018769	0.002636
N	42,578	42,578	42,578

Table 3. Regression results of the spatial lag model (SLM) and spatial error model (SEM).

Variables	2016		2018		2020	
	SLM	SEM	SLM	SEM	SLM	SEM
EEQ	−0.0170463	−0.00821829	−0.0395165	−0.0126085	−0.0116458	−0.00211267
Constant	0.128109	0.832224	0.118293	0.698749	0.135744	0.811926
Log Likelihood	34,603.153252	34,603.153252	16,438.3	16,418.297529	41,438.1	41,436.064802
Akaike info criterion	−69,230.3	−69,202.3	−32,870.7	−32,850.6	−82,876.2	−82,868.1
Schwarz criterion	−69,202.3	−69,185	−32,844.7	−32,820.5	−82,850.3	−82,850.8
R-squared	0.743941	0.743941	0.753784	0.753853	0.696779	0.696789
N	42,577	42,577	42,577	42,577	42,577	42,577

The regression coefficient of land subsidence was less than 0, indicating that an increase in the land subsidence rate led to the degradation of EEQ. Land subsidence increase was inevitably accompanied by a certain degree of urban expansion, land resource development, pollution emissions, and resource exploitation, and the intensity of such a high increase in human activities interfered with the land ecological system stability, reduce the bearing capacity of land resources, and lead to the deterioration of the ecological environment, ecological system function degradation, and ecosystem health levels. In addition, the spatial error term was also significant at the 1% level in all models, indicating that changes in ecological quality were also influenced by other factors (topography, climate, population, etc.).

Table 4. Regression results of spatial error model with lag dependence (SEMLD).

Variables	2016	2018	2020
EEQ	−0.00821829	−0.0126085	−0.00211267
Constant	0.832224	0.698749	0.811926
Log likelihood	34,618.01	16,407.297529	41,441.064802
Akaike info criterion	−69,230.3	−32,810.6	−82,868.1
Schwarz criterion	−69,185	−32,793.3	−82,850.8
R-squared	0.743903	0.753853	0.696789
N	42,578	42,578	42,578

4. Discussion

4.1. The Influence of Land Use on Land Subsidence

Land-use-type maps extracted from CLCD dataset [57] (Figure 9) showed that there were no significant land-use changes in the study area from 2016 to 2020. The results showed a high geographical proximity of urban building sites to areas of subsidence. The construction areas in three periods demonstrated the same distribution as the subsidence area. The spatial variation was concentrated in the central and northern parts of Shenmu City and near Fugu County. There was no change in land-use types in the vast majority of regions.

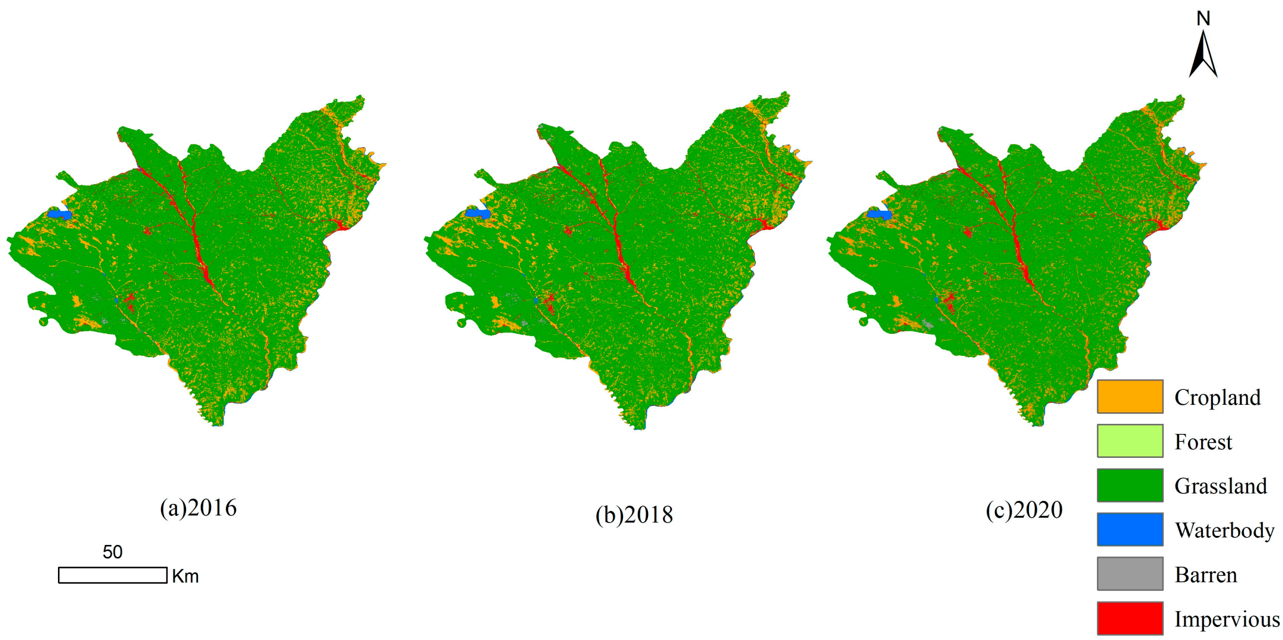

Figure 9. Land-use map (2016–2020) in Shenfu mining area.

4.2. The Influence of Nature Factors on Land Subsidence

Different natural factors influenced ground subsidence at different scales. According to the Harmonized World Soil Database (HWSD), loessal soils and aeolian sandy soils of the Shenfu mine area accounted for 37.41% and 31.02% respectively, and together account for 68.43% of the local area. The loose, soft soil texture leads to a fragile structure, reducing overall soil stability. The meteorological factors extracted from the 1 km monthly mean meteorological dataset for China [58] are shown in Figure 10. The average temperature values of 2016, 2018, 2020 were 9.0911 °C, 9.0639 °C and 8.8801 °C, respectively, which showed almost no change. Average precipitation values were 41.7608 mm, 36.9734 mm and 43.0736 mm, respectively, which demonstrated some stability. Hence, soil texture and human activity were the main causes of ground subsidence.

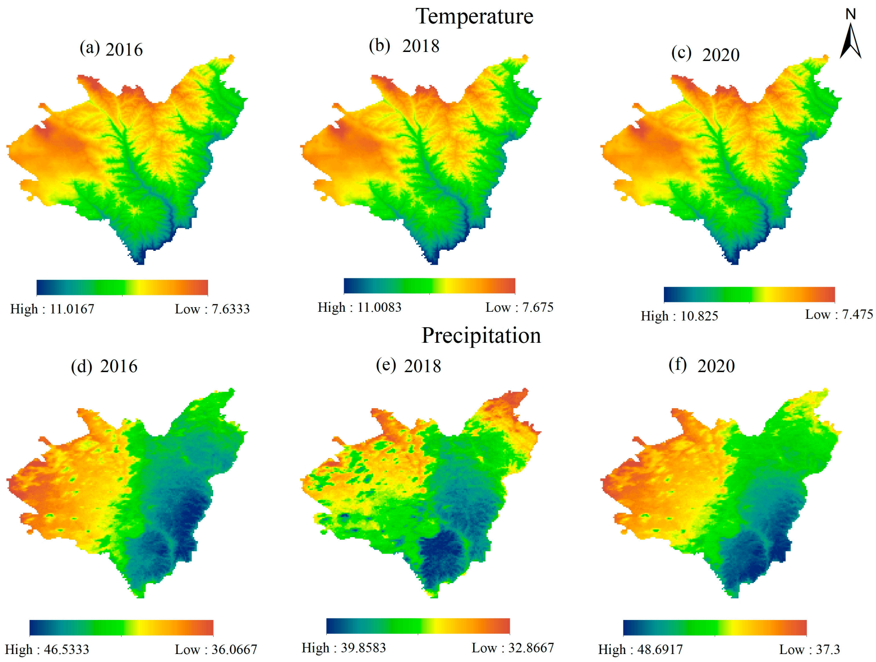

Figure 10. Average temperature and precipitation (2016–2020) in Shenfu mining area.

The land ecosystem in mining areas was very complex because its background, development, and evolution were influenced by several different factors [59]. The selection of appropriate methods and models was essential for the analysis of the spatiotemporal relationship between land subsidence and EEQ. Traditional regression methods, such as OLS regression, did not concern the spatial autocorrelation caused by several variables with spatial independence; thus, it made the results useless, leading to misleading conclusions. Therefore, spatial regression is recommended to address spatial dependence issues in land ecosystem studies. Scientifically revealing the mechanism of land subsidence regarding ecological environmental quality helped to deeply analyze the complex relationship between land subsidence and ecological environmental quality. It had significant practical value for alleviating land abandonment, declining resource-carrying capacity, and ecosystem function degradation in mining areas in China.

4.3. Implications and Suggestions

Although a spatiotemporal analysis of the spatiotemporal relationship between land subsidence and EEQ was effectively carried out to better understand the land subsidence impact mechanism on EEQ, this study had limitations that need to be additionally investigated. In the future, data validation should be conducted by comparing it with other data or relevant published datasets. Additionally, EEQ was influenced not only by its own grid elements but also by neighboring and distant grid elements. Consequently, in future work, we plan to consider the impact of other variables and investigate how land subsidence affects EEQ through direct and indirect multiscale effects.

It was recommended that the mining of mineral resources was carried out while considering the protection of the environment, placing equal emphasis on both and giving top priority to the treatment and restoration of the ecological environment in other mining areas. We strengthened the supervision of mining work and actively promoted the coordinated development of social, economic and ecological benefits. In the process of future coal resource mining, we must uphold attitude of attaching importance to ecological restoration of the local environment, strengthen the ecological restoration of the mining area after mining, especially the comprehensive restoration and treatment of the mine pit and the surrounding area, and strive to practice green development.

5. Conclusions

Land subsidence was widely distributed in the study area, with annual deformation rates ranging from −353.40 mm/year to 246.24 mm/year and average rates of 7.0176, 0.2181, and 0.2490 mm/year. The study found that the most visible subsidence areas were located in mining and urban areas. Furthermore, EEQ was spatially correlated with land subsidence, as indicated by both global and local Moran's I indices. The spatial regression model effectively captured the relationship between land subsidence and EEQ, indicating that an increase in urbanization lead to a decline in EEQ. Overall, the aggravation of land subsidence led to the deterioration of EEQ. Furthermore, the disturbance of land subsidence to EEQ gradually weakened during the study period. The results can enhance the appreciation of the spatiotemporally different interactions between land subsidence and EEQ. In addition, it can offer a possible direction for environmental protection and sustainable and green mining development planning.

Author Contributions: Conceptualization, Yonghua Zhao; methodology, Yonghua Zhao and Shuaizhi Kang; data curation, formal analysis, and software, Shuaizhi Kang; validation, Chaoqun Ma and Yonghua Zhao; investigation, Shuaizhi Kang and Yong Ao; writing—original draft preparation, Yonghua Zhao, Shuaizhi Kang; writing—review and editing, Yonghua Zhao, Shuaizhi Kang, and Xia Jia; visualization, Shuaizhi Kang and Yong Ao; supervision, Yonghua Zhao and Xia Jia; project administration and funding acquisition, Yonghua Zhao. All authors have read and agreed to the published version of the manuscript.

Funding: This research was funded by the Innovation Capability Support Program of Shaanxi (2024RS-CXTD-55).

Data Availability Statement: The data presented in this study are available on request from the corresponding author. The data are not publicly available due to privacy.

Conflicts of Interest: The authors declare no conflicts of interest.

References

1. Saedpanah, S.; Amanollahi, J. Environmental pollution and geo-ecological risk assessment of the Qhorveh mining area in western Iran. *Environ. Pollut.* **2019**, *253*, 811–820. [CrossRef] [PubMed]
2. Zhang, Y.; Feng, G.; Zhang, M.; Ren, H.; Bai, J.; Guo, Y.; Jiang, H.; Kang, L. Residual coal exploitation and its impact on sustainable development of the coal industry in China. *Energy Policy* **2016**, *96*, 534–541. [CrossRef]
3. Hu, T.; Chang, J.; Liu, X.; Feng, S. Integrated methods for determining restoration priorities of coal mining subsidence areas based on green infrastructure: –A case study in the Xuzhou urban area, of China. *Ecol. Indic.* **2018**, *94*, 164–174. [CrossRef]
4. Yang, Z.; Li, W.; Pei, Y.; Qiao, W.; Wu, Y. Classification of the type of eco-geological environment of a coal mine district: A case study of an ecologically fragile region in Western China. *J. Clean. Prod.* **2018**, *174*, 1513–1526. [CrossRef]
5. Zhang, Y.; Lian, X.; Ge, L.; Liu, X.; Du, Z.; Yang, W.; Wu, Y.; Hu, H.; Cai, Y. Surface subsidence monitoring induced by underground coal mining by combining DInSAR and UAV photogrammetry. *Remote Sens.* **2022**, *14*, 4711. [CrossRef]
6. Diao, X.; Wu, K.; Zhou, D.; Li, L. Integrating the probability integral method for subsidence prediction and differential synthetic aperture radar interferometry for monitoring mining subsidence in Fengfeng, China. *J. Appl. Remote Sens.* **2016**, *10*, 16028. [CrossRef]
7. Chen, S.; Yin, D.; Cao, F.; Liu, Y.; Ren, K. An overview of integrated surface subsidence-reducing technology in mining areas of China. *Nat. Hazards* **2016**, *81*, 1129–1145. [CrossRef]
8. Ma, C.; Cheng, X.; Yang, Y.; Zhang, X.; Guo, Z.; Zou, Y. Investigation on mining subsidence based on multi-temporal InSAR and time-series analysis of the small baseline subset—Case study of working faces 22201-1/2 in Bu'ertai mine, Shendong coalfield, China. *Remote Sens.* **2016**, *8*, 951. [CrossRef]
9. Cai, Y.; Jin, Y.; Wang, Z.; Chen, T.; Wang, Y.; Kong, W.; Xiao, W.; Li, X.; Lian, X.; Hu, H. A review of monitoring, calculation, and simulation methods for ground subsidence induced by coal mining. *Int. J. Coal Sci. Technol.* **2023**, *10*, 32. [CrossRef]
10. Yang, D.; Qiu, H.; Ma, S.; Liu, Z.; Du, C.; Zhu, Y.; Cao, M. Slow surface subsidence and its impact on shallow loess landslides in a coal mining area. *Catena* **2022**, *209*, 105830. [CrossRef]

11. Zheng, L.; Zhu, L.; Wang, W.; Guo, L.; Chen, B. Land subsidence related to coal mining in China revealed by L-band InSAR analysis. *Int. J. Environ. Res. Public Health* **2020**, *17*, 1170. [CrossRef]
12. Zhang, Y.; Wu, H.; Li, M.; Kang, Y.; Lu, Z. Investigating ground subsidence and the causes over the whole Jiangsu Province, China using sentinel-1 SAR data. *Remote Sens.* **2021**, *13*, 179. [CrossRef]
13. Osmanoğlu, B.; Sunar, F.; Wdowinski, S.; Cabral-Cano, E. Time series analysis of InSAR data: Methods and trends. *ISPRS J. Photogramm.* **2016**, *115*, 90–102. [CrossRef]
14. Karamvasis, K.; Karathanassi, V. Performance analysis of open source time series InSAR methods for deformation monitoring over a broader mining region. *Remote Sens.* **2020**, *12*, 1380. [CrossRef]
15. Lei, K.; Ma, F.; Chen, B.; Luo, Y.; Cui, W.; Zhou, Y.; Sha, T. Three-dimensional surface deformation characteristics based on time series InSAR and GPS Technologies in Beijing, China. *Remote Sens.* **2021**, *13*, 3964. [CrossRef]
16. Ma, D.; Zhao, S. Quantitative analysis of land subsidence and its effect on vegetation in Xishan coalfield of Shanxi Province. *ISPRS Int. J. Geo-Inf.* **2022**, *11*, 154. [CrossRef]
17. Jing, Z.; Wang, J.; Zhu, Y.; Feng, Y. Effects of land subsidence resulted from coal mining on soil nutrient distributions in a loess area of China. *J. Clean. Prod.* **2018**, *177*, 350–361. [CrossRef]
18. Li, H.; Zha, J.; Guo, G. A new dynamic prediction method for surface subsidence based on numerical model parameter sensitivity. *J. Clean Prod.* **2019**, *233*, 1418–1424. [CrossRef]
19. Yuan, M.; Li, M.; Liu, H.; Lv, P.; Li, B.; Zheng, W. Subsidence monitoring base on SBAS-InSAR and slope stability analysis method for damage analysis in mountainous mining subsidence regions. *Remote Sens.* **2021**, *13*, 3107. [CrossRef]
20. Wu, L.; Sun, C.; Fan, F. Estimating the characteristic spatiotemporal variation in habitat quality using the invest model—A case study from Guangdong–Hong Kong–Macao Greater Bay Area. *Remote Sens.* **2021**, *13*, 1008. [CrossRef]
21. Xu, Y.; Li, T.; Tang, X.; Zhang, X.; Fan, H.; Wang, Y. Research on the Applicability of DInSAR, Stacking-InSAR and SBAS-InSAR for Mining Region Subsidence Detection in the Datong Coalfield. *Remote Sens.* **2022**, *14*, 3314. [CrossRef]
22. Zhao, Y.; Zhou, L.; Wang, C.; Li, J.; Qin, J.; Sheng, H.; Huang, L.; Li, X. Analysis of the Spatial and Temporal Evolution of Land Subsidence in Wuhan, China from 2017 to 2021. *Remote Sens.* **2022**, *14*, 3142. [CrossRef]
23. Xu, H.; Duan, W.; Deng, W.; Lin, M. RSEI or MRSEI? Comment on Jia et al. Evaluation of Eco-Environmental Quality in Qaidam Basin Based on the Ecological Index (MRSEI) and GEE. *Remote Sens.* 2021, 13, 4543. *Remote Sens.* **2022**, *14*, 5307. [CrossRef]
24. Hu, X.; Xu, H. A new remote sensing index for assessing the spatial heterogeneity in urban ecological quality: A case from Fuzhou City, China. *Ecol. Indic.* **2018**, *89*, 11–21. [CrossRef]
25. Hang, X.; Li, Y.; Luo, X.; Xu, M.; Han, X. Assessing the ecological quality of Nanjing during its urbanization process by using satellite, meteorological, and socioeconomic data. *J. Meteorol. Res.* **2020**, *34*, 280–293. [CrossRef]
26. Xiong, Y.; Xu, W.; Lu, N.; Huang, S.; Wu, C.; Wang, L.; Dai, F.; Kou, W. Assessment of spatial–temporal changes of ecological environment quality based on RSEI and GEE: A case study in Erhai Lake Basin, Yunnan province, China. *Ecol. Indic.* **2021**, *125*, 107518. [CrossRef]
27. Zhu, D.; Chen, T.; Zhen, N.; Niu, R. Monitoring the effects of open-pit mining on the eco-environment using a moving window-based remote sensing ecological index. *Environ. Sci. Pollut. R.* **2020**, *27*, 15716–15728. [CrossRef]
28. Zhu, C.; Zhang, X.; Zhou, M.; He, S.; Gan, M.; Yang, L.; Wang, K. Impacts of urbanization and landscape pattern on habitat quality using OLS and GWR models in Hangzhou, China. *Ecol. Indic.* **2020**, *117*, 106654. [CrossRef]
29. Shi, T.; Yang, S.; Zhang, W.; Zhou, Q. Coupling coordination degree measurement and spatiotemporal heterogeneity between economic development and ecological environment—Empirical evidence from tropical and subtropical regions of China. *J. Clean. Prod.* **2020**, *244*, 118739. [CrossRef]
30. Wang, X.; Che, L.; Zhou, L.; Xu, J. Spatio-temporal dynamic simulation of land use and ecological risk in the Yangtze River Delta Urban Agglomeration, China. *Chin. Geogr. Sci.* **2021**, *31*, 829–847. [CrossRef]
31. Liu, W.; Zhan, J.; Zhao, F.; Wang, C.; Zhang, F.; Teng, Y.; Kumi, M.A. Spatio-temporal variations of ecosystem services and their drivers in the Pearl River Delta, China. *J. Clean. Prod.* **2022**, *337*, 130466. [CrossRef]
32. Wu, J.; Bai, Z. Spatial and temporal changes of the ecological footprint of China's resource-based cities in the process of urbanization. *Resour. Policy* **2022**, *75*, 102491. [CrossRef]
33. Li, H.; Peng, J.; Yanxu, L.; Yi'na, H. Urbanization impact on landscape patterns in Beijing City, China: A spatial heterogeneity perspective. *Ecol. Indic.* **2017**, *82*, 50–60. [CrossRef]
34. Ji, B.; Qin, Y.; Zhang, T.; Zhou, X.; Yi, G.; Zhang, M.; Li, M. Analyzing driving factors of drought in growing season in the Inner Mongolia based on Geodetector and GWR models. *Remote Sens.* **2022**, *14*, 6007. [CrossRef]
35. Tian, A.; Xu, T.; Gao, J.; Liu, C.; Han, L. Multi-scale spatiotemporal wetland loss and its critical influencing factors in China determined using innovative grid-based GWR. *Ecol. Indic.* **2023**, *149*, 110144. [CrossRef]
36. Xiao, W.; Fu, Y.; Wang, T.; Lv, X. Effects of land use transitions due to underground coal mining on ecosystem services in high groundwater table areas: A case study in the Yanzhou coalfield. *Land. Use Policy* **2018**, *71*, 213–221. [CrossRef]
37. Berardino, P.; Fornaro, G.; Lanari, R.; Sansosti, E. A new algorithm for surface deformation monitoring based on small baseline differential SAR interferograms. *IEEE Trans. Geosci. Remote* **2002**, *40*, 2375–2383. [CrossRef]
38. Casu, F.; Manzo, M.; Lanari, R. A quantitative assessment of the SBAS algorithm performance for surface deformation retrieval from DInSAR data. *Remote Sens. Environ.* **2006**, *102*, 195–210. [CrossRef]

39. Sun, H.; Peng, H.; Zeng, M.; Wang, S.; Pan, Y.; Pi, P.; Liu, F. Land subsidence in a coastal city based on SBAS-InSAR monitoring: A case study of Zhuhai, China. *Remote Sens.* **2023**, *15*, 2424. [CrossRef]
40. Chen, D.; Chen, H.; Zhang, W.; Cao, C.; Zhu, K.; Yuan, X.; Du, Y. Characteristics of the Residual Surface Deformation of Multiple Abandoned Mined-Out Areas Based on a Field Investigation and SBAS-InSAR: A Case Study in Jilin, China. *Remote Sens.* **2020**, *12*, 3752. [CrossRef]
41. Pu, C.; Xu, Q.; Zhao, K.; Jiang, Y.; Hao, L.; Liu, J.; Chen, W.; Kou, P. Characterizing the Topographic Changes and Land Subsidence Associated with the Mountain Excavation and City Construction on the Chinese Loess Plateau. *Remote Sens.* **2021**, *13*, 1556. [CrossRef]
42. Zhou, M.; Li, Z.; Gao, M.; Zhu, W.; Zhang, S.; Ma, J.; Ta, L.; Yang, G. Revealing the Eco-Environmental Quality of the Yellow River Basin: Trends and Drivers. *Remote Sens.* **2024**, *16*, 2018. [CrossRef]
43. Li, P.; Wang, J.; Liu, M.; Xue, Z.; Bagherzadeh, A.; Liu, M. Spatio-temporal variation characteristics of NDVI and its response to climate on the Loess Plateau from 1985 to 2015. *Catena* **2021**, *203*, 105331. [CrossRef]
44. Polykretis, C.; Grillakis, M.G.; Alexakis, D.D. Exploring the impact of various spectral indices on land cover change detection using change vector analysis: A case study of Crete Island, Greece. *Remote Sens.* **2020**, *12*, 319. [CrossRef]
45. Ermida, S.L.; Soares, P.; Mantas, V.; Göttsche, F.M.; Trigo, I.F. Google earth engine open-source code for land surface temperature estimation from the landsat series. *Remote Sens.* **2020**, *12*, 1471. [CrossRef]
46. Raynolds, M.K.; Walker, D.A. Increased wetness confounds Landsat-derived NDVI trends in the central Alaska North Slope region, 1985-2011. *Environ. Res. Lett.* **2016**, *11*, 85004. [CrossRef]
47. Wu, D. Spatially and temporally varying relationships between ecological footprint and influencing factors in China's provinces Using Geographically Weighted Regression (GWR). *J. Clean. Prod.* **2020**, *261*, 121089. [CrossRef]
48. Jing, Y.; Zhang, F.; He, Y.; Johnson, V.C.; Arikena, M. Assessment of spatial and temporal variation of ecological environment quality in Ebinur Lake Wetland National Nature Reserve, Xinjiang, China. *Ecol. Indic.* **2020**, *110*, 105874. [CrossRef]
49. Qian, D.; Yan, C.; Xing, Z.; Xiu, L. Monitoring coal mine changes and their impact on landscape patterns in an alpine region: A case study of the Muli coal mine in the Qinghai-Tibet Plateau. *Environ. Monit. Assess.* **2017**, *189*, 1–3. [CrossRef]
50. Hu, X.; Ma, C.; Huang, P.; Guo, X. Ecological vulnerability assessment based on AHP-PSR method and analysis of its single parameter sensitivity and spatial autocorrelation for ecological protection—A case of Weifang City, China. *Ecol. Indic.* **2021**, *125*, 107464. [CrossRef]
51. Li, W.; Wang, Y.; Xie, S.; Cheng, X. Coupling coordination analysis and spatiotemporal heterogeneity between urbanization and ecosystem health in Chongqing municipality, China. *Sci. Total Environ.* **2021**, *791*, 148311. [CrossRef] [PubMed]
52. Song, Y.; Wang, J.; Ge, Y.; Xu, C. An optimal parameters-based geographical detector model enhances geographic characteristics of explanatory variables for spatial heterogeneity analysis: Cases with different types of spatial data. *GISci. Remote Sens.* **2020**, *57*, 593–610. [CrossRef]
53. Chen, D.; Lu, X.; Hu, W.; Zhang, C.; Lin, Y. How urban sprawl influences eco-environmental quality: Empirical research in China by using the Spatial Durbin model. *Ecol. Indic.* **2021**, *131*, 108113. [CrossRef]
54. Chen, W.; Chi, G.; Li, J. The spatial association of ecosystem services with land use and land cover change at the county level in China, 1995–2015. *Sci. Total Environ.* **2019**, *669*, 459–470. [CrossRef]
55. Guan, W.; Xu, S. Study of spatial patterns and spatial effects of energy eco-efficiency in China. *J. Geogr. Sci.* **2016**, *26*, 1362–1376. [CrossRef]
56. Fang, C.; Liu, H.; Li, G. International progress and evaluation on interactive coupling effects between urbanization and the eco-environment. *J. Geogr. Sci.* **2016**, *26*, 1081–1116. [CrossRef]
57. Yang, J.; Huang, X. The 30 m annual land cover dataset and its dynamics in China from 1990 to 2019. *Earth Syst. Sci. Data Discuss.* **2021**, *13*, 3907–3925. [CrossRef]
58. Ding, Y.; Peng, S. Spatiotemporal Trends and Attribution of Drought across China from 1901–2100. *Sustainability* **2020**, *12*, 477. [CrossRef]
59. Hasan, S.S.; Zhen, L.; Miah, M.G.; Ahamed, T.; Samie, A. Impact of land use change on ecosystem services: A review. *Environ. Dev.* **2020**, *34*, 100527. [CrossRef]